Flux Immunity Robust Predictive Current Control With Incremental Model and Extended State Observer for PMSM Drive

Ming Yang, *Member, IEEE*, Xiaoyu Lang, Jiang Long, and Dianguo Xu, *Fellow, IEEE*

***Abstract*—A robust predictive current control algorithm for permanent magnet synchronous motor (PMSM) drives is proposed. The robust controller adopts an incremental system model, thus can operate without knowing the rotor flux, which is a pivotal parameter in conventional dead-beat control. The incremental model is easy to implement compared with relevant flux identification algorithms or observers. The robust controller adopts an extended state observer (ESO) to enhance inductance robustness to cater for the divergence caused by stator inductance mismatch. The inductance mismatch uncertainties can be estimated and compensated by ESO. Conventional dead-beat control is modified for multistep prediction to achieve high disturbance rejection. Detailed stability and disturbance rejection analysis are conducted theoretically, and rules on parameter selection are given. Comparative simulations and experimentations verify the effectiveness and superiority of proposed robust control over conventional dead-beat control.**

***Index Terms*—Disturbance rejection, extended state observer (ESO), incremental model, permanent magnet synchronous motor (PMSM) drives, predictive control, robustness.**

NOMENCLATURE

R	Stator resistance.
L_d, L_q	Stator inductance (d, q axis, respectively).
$L_{\rm PPC}$	Inductance parameter used in PPC.
$L_{\rm R-PPC}$	Inductance parameter used in R-PPC.
$\psi_{\rm f-PPC}$	Rotor flux linkage used in PPC.
$R_{\rm PPC}$, $R_{\rm R-PPC}$	Stator resistance used in PPC and R-PPC.
ψ_f	Rotor flux linkage.
u_d, u_q	Stator voltage (d, q axis, respectively).
i_d, i_q	Stator current (d, q axis, respectively).
ω_e	Electrical rotor speed.
T	Sampling period of current-loop.
k	Sample.
T_e	Electromagnetic torque.
T_L	Load torque.
Δ	Symbol of increment.
ω_c	Bandwidth of ESO.
c_1, c_2	Gains of ESO.
$\mathbf{k}_1$, $\mathbf{k}_2$	States of ESO.
$.^{ref}$	Reference value.
$\hat{}$	Estimated value.

Manuscript received June 21, 2016; revised October 13, 2016; accepted January 4, 2017. Date of publication January 17, 2017; date of current version August 2, 2017. This work was supported by the Project Self-Planned Task (No. SKLRS201610B) of State Key Laboratory of Robotics and System (Harbin Institute of Technology). Recommended for publication by Associate Editor G. Escobar.

The authors are with the School of Electrical Engineering and Automation, Harbin Institute of Technology, Harbin 150001, China (e-mail: yangming_hit@163.com; langxiaoyu@163.com; volkswage.n@163.com; xudiang@hit.edu.cn).

Color versions of one or more of the figures in this paper are available online at http://ieeexplore.ieee.org.

Digital Object Identifier 10.1109/TPEL.2017.2654540

I. INTRODUCTION

PERMANENT magnet synchronous motors (PMSMs) are widely used in industrial products, such as numerical control machines, industrial robots, and electric vehicles due to significant advantages such as high power-weight ratio, small volume, and simple structure. These application fields require rapid electrical torque response, thus fast dynamic performance is fundamental for a PMSM drive [1]–[4]. Since dynamic current response is responsible of dynamic torque performance, a fast current-loop is required for fulfilling mechanical requirements. Many current control methods have been developed, such as hysteresis control [33], [34], direct torque control [5], sliding mode [35], predictive current control [6]–[10], and the combination of these concepts [11]–[13].

Among controllers, predictive controllers offer the fastest response [36]. Predictive control techniques can be divided into two categories: finite control set model predictive control [14]–[16] and dead-beat control [17]–[20]. Because pulse-width modulation (PWM) is adopted in dead-beat control to translate control voltages into switching signals, dead-beat control is denoted as PWM predictive control (PPC) in this paper. PPC appears a suitable precise method for a PMSM drive due to its modulation module, which guarantees fast dynamics and low current ripple. Since PPC is based on a system model, its performance largely depends on the accuracy of model parameters, especially the stator inductance and rotor flux. This motor parameter accuracy tends to limit industrial application. Thus, a robust and easy-implemented modification to PPC is required.

In a PMSM, the rotor flux is equal to the permanent magnet flux linkage. If the rotor flux used in the controller mismatches the real flux, static error or oscillation of the current will occur. However, rotor flux is difficult to measure directly, plus for a ferrite-based magnet, a 20% flux reduction occurs per 100 °C ambient temperature increase [41]. Since PMSM applications differ, rotor flux reductions vary. This produces errors in the back electromotive force (EMF) calculation or deteriorates PPC

performance when using a fixed flux value instead of an online estimation of rotor flux. Thus, the main approach to improve flux robustness is based on identification. Many flux estimation methods have been investigated [21]–[27], [37]. In [22], position offset based parameter estimation is used to estimate rotor flux, along with some other mechanical parameters. In [37], a Kalman filter and Luenberger observer were used to estimate rotor variables to improve the performance of predictive current control, and satisfactory results were obtained. Another strategy based on injecting flux weakening current ($i_d \neq 0$) to estimate flux was presented in [23] and [24]. The main disadvantage is that accuracy is influenced by the nonlinearity typical of a voltage-source inverter (VSI). In [25] and [26], distorted voltage compensation due to VSI nonlinearity is incorporated to achieve flux estimation. In [27], an integration method was proposed to eliminate the *q*-axis current static error caused by flux mismatch, but the strategy impairs dynamic response. The disadvantages of identification are dependent on accurate voltage and current measurement. Also, identification techniques are complex to practically implement.

Inductance mismatch is also common and some methods [28]–[31] present effective solutions. In [28], novel robustness designs were proposed to diminish the current oscillation caused by large controller inductance, but the system bandwidth is lowered. A model reference adaptive method is adopted in [29] and [30], which effectively attenuates the error between the current reference and the feedback. In [31], a predictive current controller combined with a Luenberger observer was proposed to mitigate parameter uncertainty influence. But the focus was more on converter uncertainty than stator inductance. These approaches that aim to enhance inductance robustness are also complex, and none combined an incremental model.

Extended state observer (ESO) proposed in [40] has advantages over conventional observers, such as independence from mathematical model accuracy, robustness, and good dynamic performance. ESO can estimate the unknown disturbance caused by inductance mismatch with high accuracy. Also only observer gains need to be tuned and the tuning process is not complicated, because the gains are determined by the desired observer bandwidth. Therefore, ESO can realize robustness against inductance mismatch and variation without complex observer tuning.

In order to eliminate rotor flux effects, with improved robustness against inductance mismatch and load disturbance, this paper proposes a robust PPC (R-PPC) algorithm, which has three main advantages. First, R-PPC adopts an incremental model, thus can operate without rotor flux. This modification improves flux robustness and avoids sophisticated flux identification methods or observers. Thus, it is readily applicable in practical applications. Second, R-PPC improves resilience to load disturbance compared to conventional PPC by applying multistep prediction to R-PPC. Third, it combines an incremental model with an ESO, which estimates the error caused by inductance uncertainty and compensates this in the prediction model.

This paper is organized as follows. Conventional PPC is introduced in Section II. The R-PPC design is demonstrated in Section III. Then stability and disturbance rejection ability are analyzed in Section IV. Section V verifies the effectiveness of the proposed R-PPC algorithm through simulations and experimentations on a 750 W PMSM servo platform. Section VI draws conclusion.

II. Conventional PWM Predictive Control

The PMSM in this paper consists of three windings (one per phase) on the stator and permanent magnets mounted on the rotor surface. The stator windings are sinusoidally distributed and displaced by 120°. Neglecting iron saturation, the voltage state-space equation of the rotor reference frame is

$$\begin{cases} \frac{di_d}{dt} = -\frac{R}{L_d} i_d + \frac{L_q}{L_d}\omega_e i_q + \frac{1}{L_d} u_d \\ \frac{di_q}{dt} = -\frac{R}{L_q} i_q - \frac{L_d}{L_q}\omega_e i_d - \frac{\psi_f \omega_e}{L_q} + \frac{1}{L_q} u_q \end{cases}. \tag{1}$$

The PMSM parameters and variables in (1) are defined in the Nomenclature. For this surface-mounted PMSM (SPMSM), $L_d = L_q = L$.

If the current-loop sampling period T is short enough, the rotor position in a sampling period can be considered constant. Then, the PMSM can be modeled in a discrete form using the first-order Taylor expansion. The discrete equation is

$$\mathbf{x}(k+1) = \mathbf{A}(k)\mathbf{x}(k) + \mathbf{B}\mathbf{u}(k) + \mathbf{d}(k) \tag{2}$$

where

$$\mathbf{x}(k) = \begin{bmatrix} i_d(k) & i_q(k) \end{bmatrix}^T \qquad \mathbf{u}(k) = \begin{bmatrix} u_d(k) & u_q(k) \end{bmatrix}^T$$

$$\mathbf{A}(k) = \begin{bmatrix} 1 - \frac{TR}{L} & T\omega_e(k) \\ -T\omega_e(k) & 1 - \frac{TR}{L} \end{bmatrix} \qquad \mathbf{B} = \begin{bmatrix} \frac{T}{L} & 0 \\ 0 & \frac{T}{L} \end{bmatrix}$$

$$\mathbf{d}(k) = \begin{bmatrix} 0 \\ \frac{-T\psi_f \omega_e(k)}{L} \end{bmatrix}.$$

In conventional PPC, optimal control voltages should regulate currents to track their reference in a single sampling period due to deadbeat characteristics. Through transformation of the discrete state (2), optimal control voltages are obtained using the following equation, in which the **B** matrix is invertible:

$$\mathbf{u}(k) = \mathbf{B}^{-1}\left[x^{ref}(k+1) - \mathbf{A}(k)\mathbf{x}(k) - \mathbf{d}(k)\right] \tag{3}$$

where $\mathbf{x}^{ref}(k+1) = \begin{bmatrix} {i_d}^{ref}(k+1) & {i_q}^{ref}(k+1) \end{bmatrix}^T$.

From (3), the prediction horizon of PPC is 1. The calculation of *dq*-axis voltage vectors is based on reference currents, stator currents, rotor position, and rotor speed. PWM transforms the control voltages into specific duty cycles. Through modulation, PPC guarantees a fixed switching frequency and low current ripple. Within a single sampling period, the actual current follows its reference. The *q*-axis current reference $i_q^{ref}(k+1)$ equals the speed-loop controller output, and for SPMSM, $i_d^{ref}(k+1)$ is set to 0.

III. Design of the Robust PWM Predictive Controller

In this section, conventional PPC is improved to eliminate the effect of rotor flux, and improve robustness against load

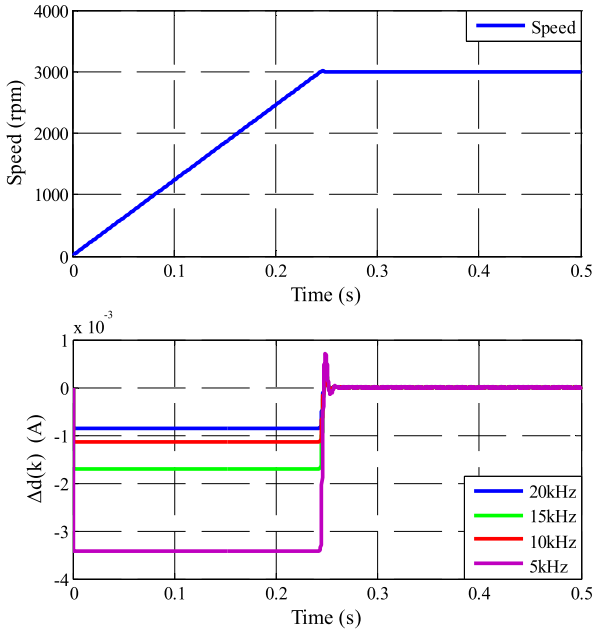

Fig. 1. Values of $\Delta\mathbf{d}(k)$ in speed transient and steady process versus different current-loop sampling frequencies for SPMSM of Table I.

disturbances and inductance mismatch. This robust PPC algorithm will be referred to as R-PPC.

A. Elimination of Rotor Flux

Rotor flux is a pivotal parameter since back EMF is $K_e\omega_e$, where K_e is back EMF coefficient and K_e is proportional to rotor's flux ψ_f. From (2), rotor flux ψ_f only appears in matrix $\mathbf{d}(k)$. In order to eliminate the effect of rotor flux, considering the incremental form of the state equation

$$\Delta\mathbf{x}(k+1) = \mathbf{A}(k)\Delta\mathbf{x}(k) + \mathbf{B}\Delta\mathbf{u}(k) + \Delta\mathbf{d}(k). \quad (4)$$

In a steady-state process, the electrical rotor speed ω_e is constant, thus the increment of $\mathbf{d}(k)$ is as follows:

$$\begin{aligned}\Delta\mathbf{d}(k) &= \begin{bmatrix} 0 \\ \frac{-T\psi_f}{L}\Delta\omega_e(k) \end{bmatrix} \\ &= \begin{bmatrix} 0 \\ \frac{-T\psi_f}{L}\left(\omega_e(k) - \omega_e(k-1)\right) \end{bmatrix} \approx \begin{bmatrix} 0 \\ 0 \end{bmatrix}. \end{aligned} \quad (5)$$

In a transient process, especially a speed step process, the electrical speed ω_e varies rapidly. However, since mechanical dynamics are much slower than electrical dynamics, the rotor speed can still be considered constant during successive current-loop sampling periods. Fig. 1 demonstrates the values of $\Delta\mathbf{d}(k)$ with different current-loop sampling frequencies, and the sampling frequency of the speed-loop is 1 kHz, as in the experimentation. The figure shows $\Delta\mathbf{d}(k)$ decreases as the current-loop sampling frequency increases. Even with a relatively low sampling frequency of 5 kHz, $\Delta\mathbf{d}(k)$ remains significantly small. Therefore, $\Delta\mathbf{d}(k) \approx 0$ is valid in both transient and steady processes, so the rotor flux ψ_f has minimal influence in the incremental model.

The PMSM is a nonlinear, strongly coupled system. Through an incremental algorithm, $\mathbf{A}(k)$ can also be assumed unchanged between successive sampling periods, so the system can be considered linear. For a linear system, the state equation is equivalent to the incremental state equation, which is

$$\begin{aligned}\underbrace{\begin{bmatrix} \Delta i_d(k+1) \\ \Delta i_q(k+1) \end{bmatrix}}_{\Delta\mathbf{x}(k+1)} &= \underbrace{\begin{bmatrix} i_d(k+1) \\ i_q(k+1) \end{bmatrix} - \begin{bmatrix} i_d(k) \\ i_q(k) \end{bmatrix}}_{\mathbf{x}(k+1)-\mathbf{x}(k)} \\ &= \underbrace{\mathbf{A}\begin{bmatrix} \Delta i_d(k) \\ \Delta i_q(k) \end{bmatrix}}_{\mathbf{A}\Delta\mathbf{x}(k)} + \underbrace{\mathbf{B}\begin{bmatrix} \Delta u_d(k) \\ \Delta u_q(k) \end{bmatrix}}_{\mathbf{B}\Delta\mathbf{u}(k)}. \end{aligned} \quad (6)$$

In (6), $\mathbf{d}(k)$, the unique matrix incorporates rotor flux, is ignored. Thus, the incremental state equation leads to an algorithm without rotor flux. Such a method does not rely on any additional observer or identification strategy. Therefore, the incremental model is easier to be implemented than flux observers in practical application.

B. Enhancement of Disturbance Rejection Ability

An incremental model has been adopted to eliminate rotor flux. The prediction horizon of conventional PPC is 1 as mentioned. In order to further improve disturbance rejection ability, the prediction horizon should be increased. More consideration of disturbances will be included in R-PPC with a larger prediction horizon, but a larger prediction horizon will increase the computational burden, possibly beyond the computing ability of the DSP.

Assuming the prediction horizon of R-PPC is p. According to [6] and [38], a 2-beat digital delay exists in the servo system. Thus, the prediction horizon is suggested to be larger than 2 to incorporate more information which is not affected by the digital delay. Therefore, considering DSP implementation, p is chosen as 3 in R-PPC, which can guarantee both accurate prediction and acceptable computational effort.

In this paper, the control horizon is chosen as 1, which may appear limiting. However, based on [38], any input signal after the $(k+1)$th instant has no influence on dq-axis currents before $(k+3)$th instant, inside which the prediction horizon is 3. Since control horizon is less than the prediction horizon and the predicting process needs all the control inputs within the prediction horizon, control voltages remain unchanged beyond the control horizon. Thus, it follows:

$$\Delta\mathbf{u}(k+p) = \Delta\mathbf{u}(k+p-1) = \Delta\mathbf{u}(k+1) = 0. \quad (7)$$

Besides multistep prediction, another modification is that currents at the $(k-1)$th instant are introduced into R-PPC for improving the antidisturbance capability, and this will be verified in Section IV-B. Taking the common parts of the forecast value of $\mathbf{x}(k-1)$ and $\mathbf{x}(k)$ into consideration amounts to the forecast value $\mathbf{x}(k+1|k-1)$, $\mathbf{x}(k+2|k-1)$, $\mathbf{x}(k+1|k)$, and $\mathbf{x}(k+2|k)$, since $p=3$. Currents and speed at the kth and $(k-1)$th

instants can be measured. The prediction equation is derived as follows:

$$\begin{cases} \mathbf{Y}_{k-1} = \mathbf{S}_{u,\,k-1}\Delta\mathbf{u}(k-1) + \mathbf{S}_{x,\,k-1}\Delta\mathbf{x}(k-1) \\ \qquad\qquad + \mathbf{E}\mathbf{x}(k-1) \\ \mathbf{Y}_k = \mathbf{S}_{u,\,k}\Delta\mathbf{u}(k) + \mathbf{S}_{x,\,k}\Delta\mathbf{x}(k) + \mathbf{E}\mathbf{x}(k) \end{cases} \tag{8}$$

where

$$\mathbf{E} = [I_{2\times2} \quad I_{2\times2}]^T{}_{4\times2} \qquad \mathbf{Y}_{k-1} = \begin{bmatrix} \mathbf{x}(k+1|k-1) \\ \mathbf{x}(k+2|k-1) \end{bmatrix}_{4\times1}$$

$$\mathbf{Y}_k = \begin{bmatrix} \mathbf{x}(k+1|k) \\ \mathbf{x}(k+2|k) \end{bmatrix}_{4\times1}$$

$$\mathbf{S}_{u,k-1} = \begin{bmatrix} \mathbf{AB}+\mathbf{B} \\ \mathbf{A}^2\mathbf{B}+\mathbf{AB}+\mathbf{B} \end{bmatrix}_{4\times2} \qquad \mathbf{S}_{u,k} = \begin{bmatrix} \mathbf{B} \\ \mathbf{AB}+\mathbf{B} \end{bmatrix}_{4\times2}$$

$$\mathbf{S}_{x,k-1} = \begin{bmatrix} \mathbf{A}^2+\mathbf{A} \\ \mathbf{A}^3+\mathbf{A}^2+\mathbf{A} \end{bmatrix}_{4\times2} \qquad \mathbf{S}_{x,k} = \begin{bmatrix} \mathbf{A} \\ \mathbf{A}^2+\mathbf{A} \end{bmatrix}_{4\times2}$$

where I is identity matrix. $\mathbf{A}$ and $\mathbf{B}$ are shown in (2).

C. Calculation of Optimal Voltage

Since the proposed R-PPC is a current-loop controller, the main goal is the stator current can accurately follow the current reference. Then, the cost function is chosen as

$$J = \left\|\alpha\mathbf{Y}_{k-1} + \beta\mathbf{Y}_k - \mathbf{I}^{ref}\right\|^2\mathbf{Q}. \tag{9}$$

In (9), α and β are weighing factors of the predictive states $\mathbf{Y}_{k-1}$ and $\mathbf{Y}_k$, respectively, and $\alpha + \beta = 1$. Matrices $\mathbf{Y}_{k-1}$ and $\mathbf{Y}_k$ are shown in (8). Other matrices in (9) are

$$\begin{cases} \mathbf{I}^{ref} = [{i_d}^{ref}(k+1), {i_q}^{ref}(k+1), {i_d}^{ref}(k+2), {i_q}^{ref} \\ \qquad (k+2)]^T_{4\times1} \text{reference currents;} \\ \mathbf{Q} = \text{diag}(q_1,\ q_2,\ q_3,\ q_4)_{4\times4} \text{ weighting factors of currents} \\ \qquad \text{at } k\text{th and } (k-1)\text{th sampling instants.} \end{cases}$$

The priority of the R-PPC controller is to compute an optimal voltage vector increment which can minimize the cost function

$$\min_{\Delta\mathbf{u}(k)} J(\mathbf{x}(k),\ \Delta\mathbf{x}(k), \Delta\mathbf{u}(k)). \tag{10}$$

In order to solve the optimization problem, an instrumental variable is defined according to cost function (9)

$$\rho = (\alpha\mathbf{Y}_{k-1} + \beta\mathbf{Y}_k - \mathbf{I}_{\text{ref}})_{4\times1}. \tag{11}$$

Then, the cost function is

$$J(\mathbf{x}(k), \Delta\mathbf{x}(k), \Delta\mathbf{u}(k)) = \rho^T\mathbf{Q}\rho. \tag{12}$$

Substituting (8) into (11), ρ can be expressed as

$$\begin{aligned} \rho =\ & \beta\mathbf{S}_{u,k}\Delta\mathbf{u}(k) - \begin{Bmatrix} \mathbf{I}_{\text{ref}} - \beta\left(\mathbf{S}_{x,k}\Delta\mathbf{x}(k) + \mathbf{E}\mathbf{x}(k)\right) \\ -\alpha\left(\mathbf{S}_{u,k-1}\Delta\mathbf{u}(k-1) + \mathbf{S}_{x,k-1}\right. \\ \times\ \left.\Delta\mathbf{x}(k-1) + \mathbf{E}\mathbf{x}(k-1)\right) \end{Bmatrix} \\ =\ & \mathbf{G}\Delta\mathbf{u}(k) - \mathbf{H}(k). \end{aligned} \tag{13}$$

The extreme condition of the cost function J can be obtained

$$\frac{\partial J}{\partial\Delta\mathbf{u}(k)} = \frac{\partial\rho^T\mathbf{Q}\rho}{\partial\Delta\mathbf{u}(k)} = 2\mathbf{G}^T\mathbf{Q}\left(\mathbf{G}\Delta\mathbf{u}(k) - \mathbf{H}(k)\right) = 0$$

$$\Rightarrow \Delta\mathbf{u}(k) = \left(\mathbf{G}^T\mathbf{Q}\mathbf{G}\right)^{-1}\mathbf{G}^T\mathbf{Q}\mathbf{H}(k). \tag{14}$$

The second order partial derivative of J is

$$\frac{\partial^2 J}{\partial\Delta\mathbf{u}(k)^2} = 2\mathbf{G}^T\mathbf{Q}\mathbf{G} > 0. \tag{15}$$

Since the second-order partial derivative is positive, $\Delta\mathbf{u}(k) = (\mathbf{G}^T\mathbf{Q}\mathbf{G})^{-1}\mathbf{G}^T\mathbf{Q}\mathbf{H}(k)$ is the optimal voltage vector increment which minimizes the cost function. According to (13), $\Delta\mathbf{u}(k)$ at kth instant can be expressed as

$$\Delta\mathbf{u}(k) = \frac{1}{\beta}\left[{\mathbf{S}_{u,k}}^T\mathbf{Q}\mathbf{S}_{u,k}\right]^{-1}{\mathbf{S}_{u,k}}^T\mathbf{Q}\mathbf{H}(k). \tag{16}$$

In (16), $\mathbf{H}(k)$ is shown as follows, according to (13)

$$\begin{aligned} \mathbf{H}(k) = \mathbf{I}_{\text{ref}} &- \alpha\mathbf{S}_{x,k-1}\Delta\mathbf{x}(k-1) - \alpha\mathbf{S}_{u,k-1}\Delta\mathbf{u}(k-1) \\ &- \alpha\mathbf{E}\mathbf{x}(k-1) - \beta\mathbf{S}_{x,k}\Delta\mathbf{x}(k) - \beta\mathbf{E}\mathbf{x}(k). \end{aligned} \tag{17}$$

It consists of two parts: feedforward compensation based on the future reference $\mathbf{I}^{ref}$, and state feedback compensation. Thus, R-PPC has a "feedforward-feedback" structure, which can quickly reduce the negative influence caused by disturbance and guarantee stability of the closed-loop system.

All the matrices in (16) and (17) are shown in (8) and (9). Then, the final control voltage of R-PPC at the kth instant is

$$\mathbf{u}(k) = \mathbf{u}(k-1) + \Delta\mathbf{u}(k) \tag{18}$$

where $\mathbf{u}(k-1)$ is the control voltage at the $(k-1)$th instant, and $\Delta\mathbf{u}(k)$ is optimal voltage increment calculated by (16) and (17).

Some critical issues about $\mathbf{I}^{ref}$ and the $\mathbf{Q}$ matrices should be discussed. The current reference at the $(k+1)$th instant $i_q^{ref}(k+1)$ is obtained from the speed-loop controller output. For an SPMSM, i_d is often controlled as 0, then $i_d^{ref}(k+1) = 0$. Since the sampling period of current-loop is small, the current reference at the $(k+2)th$ instant can be assumed approximately equal to the $(k+1)$th instant. Then, $i_q^{ref}(k+2) = i_q^{ref}(k+1)$, $i_d^{ref}(k+2) = i_d^{ref}(k+1) = 0$.

q_1, q_2, q_3, and q_4 in the $\mathbf{Q}$ matrix represent the weighting factors of $i_d(k-1)$, $i_q(k-1)$, $i_d(k)$, and $i_q(k)$, respectively. According to [39], $i_d(k-1)$, $i_q(k-1)$, $i_d(k)$, and $i_q(k)$ all have the same nature (same unit and order of magnitude) and the cost function shown as (9) can be categorized as cost functions without weighting factors. Therefore, no weighting factors and their corresponding tuning process are necessary. In other words, the importance of q_1, q_2, q_3, and q_4 is the same, so for simplicity, the $\mathbf{Q}$ matrix is set as an identity matrix.

D. Design of Extended State Observer

Conventional PPC produces static error, or even unstable oscillation of the currents, if the parameters in predictive controller do not match the real motor parameters. According to [27], armature resistance R can be neglected in predicting (2), while

stator inductance L is critical to system stability. [28] established that when inductance in PPC is more than double of real value, current oscillation and system divergence will occur. Therefore, to eliminate the negative impact caused by inductance mismatch and to improve robustness against inductance variation, an ESO is incorporated.

In order to analyze the influence of inductance mismatch, (1) can be changed to

$$\begin{cases} \frac{di_d}{dt} = -\frac{R}{L_0+\Delta L} i_d + \omega_e i_q + \frac{1}{L_0+\Delta L} u_d \\ \frac{di_q}{dt} = -\frac{R}{L_0+\Delta L} i_q - \omega_e i_d - \frac{\psi_f \omega_e}{L_0+\Delta L} + \frac{1}{L_0+\Delta L} u_q \end{cases} \tag{19}$$

where ΔL is the inductance mismatch and L_0 is the nominal inductance value. Equation (19) can be changed to a predictive state equation:

$$\dot{\mathbf{x}}(t) = \mathbf{A}\mathbf{x}(t) + \mathbf{B}\mathbf{u}(t) + \mathbf{d}(t) + \mathbf{B}\mathbf{u}_m(t) \tag{20}$$

where $\mathbf{u}_m(t)$ represents the equivalent *dq*-axis voltage error caused by inductance mismatch and its effect can be compensated if $\mathbf{u}_m(t)$ can be estimated by the ESO.

The voltage error caused by inductance mismatch can be extended as a new state in the ESO. This means the mismatch effect can be obtained through a feedback structure in the ESO. The ESO is independent of the system mathematical model and has strong robustness. Thus, the ESO is suitable to estimate motor currents with inductance mismatch.

According to (20), the ESO can be designed as follows:

$$\begin{cases} \dot{\mathbf{k}}_1(t) = \mathbf{k}_2(t) + \mathbf{A}\mathbf{x}(t) + \mathbf{B}\mathbf{u}(t) + \mathbf{d}(t) + c_1[\mathbf{x}(t) - \mathbf{k}_1(t)] \\ \dot{\mathbf{k}}_2(t) = c_2\left[\mathbf{x}(t) - \mathbf{k}_1(t)\right] \end{cases} \tag{21}$$

where $\boldsymbol{k}_1$ and $\boldsymbol{k}_2$ are two states of the ESO, c_1 and c_2 are the ESO gains. $\mathbf{k}_1(t) \rightarrow \mathbf{x}(t)$ and $\mathbf{k}_2(t) \rightarrow \mathbf{B}\mathbf{u}_m(t)$, where the dimension of $\mathbf{k}_1(t)$ and $\mathbf{k}_2(t)$ are both 2×1. $\mathbf{k}_1(t)$ and $\mathbf{u}_m(t)$ generated by ESO are denoted as

$$\mathbf{k}_1(t) = \begin{bmatrix} \hat{i}_d(t) & \hat{i}_q(t) \end{bmatrix}^T \quad \mathbf{u}_m(t) = [u_{d\_\text{error}} \quad u_{q\_\text{error}}]^T$$

where $\hat{i}_d(t)$ and $\hat{i}_q(t)$ are the estimated *dq*-axis currents; u_{d_error} and u_{q_error} are the equivalent voltage errors at *dq*-axis caused by inductance mismatch.

The discrete form of (21) can be obtained through a one-order Taylor expression

$$\begin{cases} \mathbf{k}_1(k+1) = (1 - Tc_1)\mathbf{k}_1(k) + T[\mathbf{k}_2(k) + \mathbf{A}\mathbf{x}(k) \\ \qquad\qquad + \mathbf{B}\mathbf{u}(k) + c_1\mathbf{x}(k)] + T\mathbf{d}(k) \\ \mathbf{k}_2(k+1) = \mathbf{k}_2(k) + Tc_2\left[\mathbf{x}(k) - \mathbf{k}_1(k)\right]. \end{cases} \tag{22}$$

In order to eliminate the effect of rotor flux which appears in $\mathbf{d}(k)$, state (22) is also changed into an incremental form. Since $\Delta\mathbf{d}(k) \approx 0$ has been established in part **A**, the incremental state equation of the ESO can be expressed as

$$\begin{cases} \Delta\mathbf{k}_1(k+1) = T[\Delta\mathbf{k}_2(k) + \mathbf{A}\Delta\mathbf{x}(k) + \mathbf{B}\Delta\mathbf{u}(k) \\ \qquad\qquad + c_1\Delta\mathbf{x}(k)] + (1 - Tc_1)\Delta\mathbf{k}_1(k) \\ \Delta\mathbf{k}_2(k+1) = \Delta\mathbf{k}_2(k) + Tc_2\left[\Delta\mathbf{x}(k) - \Delta\mathbf{k}_1(k)\right]. \end{cases} \tag{23}$$

Therefore, in (17), $\mathbf{x}(k)$, $\Delta\mathbf{x}(k)$, and $\Delta\mathbf{u}(k-1)$ are substituted by $\mathbf{k}_1(k)$, $\Delta\mathbf{k}_1(k)$, and $\Delta\mathbf{u}(k-1) + \mathbf{B}^{-1}\Delta\mathbf{k}_2(k-1)$, respectively, then (17) is converted to

$$\begin{aligned} \mathbf{H}'(k) = \ & \mathbf{I}_{\text{ref}} - \alpha\mathbf{S}_{x,k-1}\Delta\mathbf{k}_1(k-1) - \alpha\mathbf{E}\mathbf{k}_1(k-1) \\ & - \beta\mathbf{S}_{x,k}\Delta\mathbf{k}_1(k) - \alpha\mathbf{S}_{u,k-1}[\Delta\mathbf{u}(k-1) \\ & + \mathbf{B}^{-1}\Delta\mathbf{k}_2(k-1)] - \beta\mathbf{E}\mathbf{k}_1(k). \end{aligned} \tag{24}$$

Then, optimal voltage increment $\Delta\mathbf{u}(k)$ is still computed through (16), while $\mathbf{H}(k)$ is replaced by $\mathbf{H}'(k)$. Finally, the optimal voltage $\mathbf{u}(k)$ is input into the SVPWM module.

IV. Performance Analysis of the System With R-PPC

The PMSM drive system structure diagram with R-PPC controller is shown in Fig. 2. The proposed R-PPC strategy is used to substitute conventional PPC to gain better parameter robustness. i_d and i_q are provided for the ESO in order to generate the equivalent voltage errors caused by inductance mismatch. The equivalent voltage errors and observed *dq*-axis currents are used in the current prediction. The predictive currents are used to calculate the optimal control voltage. After calculation, optimal voltage references are generated, and these voltages are transferred into specific switching signals using SVPWM module.

A. Stability Analysis

First, the stability of the ESO is analyzed, since this is the foundation of the stability of whole system because the ESO provides estimated states for current prediction. Then, (20) can be changed into the following form:

$$\begin{bmatrix} \dot{\mathbf{x}}(t) \\ \mathbf{B}\dot{\mathbf{u}}_m(t) \end{bmatrix} = \begin{bmatrix} \mathbf{A} & 1 \\ 0 & 0 \end{bmatrix} \begin{bmatrix} \mathbf{x}(t) \\ \mathbf{B}\mathbf{u}_m(t) \end{bmatrix} + \begin{bmatrix} \mathbf{B}\mathbf{u}(t) \\ 0 \end{bmatrix} + \begin{bmatrix} \mathbf{d}(t) \\ \mathbf{B}f(t) \end{bmatrix} \tag{25}$$

where $\mathbf{B}f(t)$ is the changing rate of $\mathbf{B}\mathbf{u}_m(t)$. Then, (21) can be expressed as

$$\begin{aligned} \begin{bmatrix} \dot{\mathbf{k}}_1(t) \\ \dot{\mathbf{k}}_2(t) \end{bmatrix} = & \begin{bmatrix} -c_1 & 1 \\ -c_2 & 0 \end{bmatrix} \begin{bmatrix} \mathbf{k}_1(t) \\ \mathbf{k}_2(t) \end{bmatrix} + \begin{bmatrix} c_1\mathbf{x}(t) + \mathbf{A}\mathbf{x}(t) \\ c_2\mathbf{x}(t) \end{bmatrix} \\ & + \begin{bmatrix} \mathbf{B}\mathbf{u}(t) \\ 0 \end{bmatrix} + \begin{bmatrix} \mathbf{d}(t) \\ \mathbf{B}f(t) \end{bmatrix}. \end{aligned} \tag{26}$$

The error between the two state equations can be obtained by subtracting (25) from (26)

$$\begin{bmatrix} \dot{\mathbf{k}}_1(t) - \dot{\mathbf{x}}(t) \\ \dot{\mathbf{k}}_2(t) - \mathbf{B}\dot{\mathbf{u}}_m(t) \end{bmatrix} = \begin{bmatrix} -c_1 & 1 \\ -c_2 & 0 \end{bmatrix} \begin{bmatrix} \mathbf{k}_1(t) - \mathbf{x}(t) \\ \mathbf{k}_2(t) - \mathbf{B}\mathbf{u}_m(t) \end{bmatrix}. \tag{27}$$

Substituting $\mathbf{k}_1(t) - \mathbf{x}(t)$ and $\mathbf{k}_2(t) - \mathbf{B}\mathbf{u}_m(t)$ as $\mathbf{e}_1(t)$ and $\mathbf{e}_2(t)$, respectively. Then, error state equation can be obtained

$$\begin{bmatrix} \dot{\mathbf{e}}_1(t) \\ \dot{\mathbf{e}}_2(t) \end{bmatrix} = \begin{bmatrix} -c_1 & 1 \\ -c_2 & 0 \end{bmatrix} \begin{bmatrix} \mathbf{e}_1(t) \\ \mathbf{e}_2(t) \end{bmatrix}. \tag{28}$$

According to Hurwitz stability criterion, the ESO will be stable if $c_1, c_2 > 0$. In [32], an ESO parameter selection method is presented, where $c_1 = 2\omega_c, c_2 = \omega_c^2$ where ω_c is the desired ESO bandwidth.

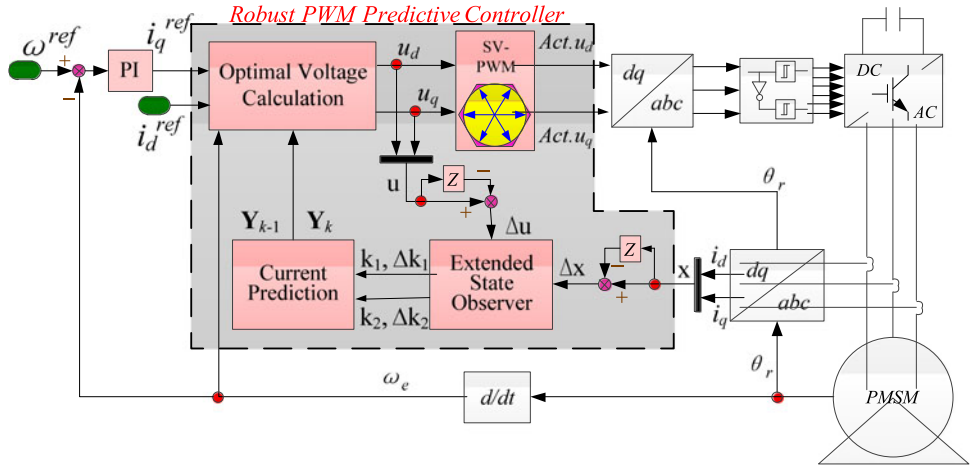

Fig. 2. Structure of the PMSM drive system with the R-PPC controller.

On the basis of a stable ESO, R-PPC stability can be evaluated. In (16), let $\frac{1}{\beta}[\mathbf{S}_{u,k}{}^T\mathbf{Q}\mathbf{S}_{u,k}]^{-1}\mathbf{S}_{u,k}{}^T\mathbf{Q} = \mathbf{K}_{\mathrm{pc}}$ and the dimension of $\mathbf{K}_{\mathrm{pc}}$ is 2×4. Then, the incremental state equation can be formulated as

$$\begin{aligned}\Delta\mathbf{x}(k+1) &= \mathbf{A}\Delta\mathbf{x}(k) + \mathbf{B}\Delta\mathbf{u}(k) \\ &= (\mathbf{A} - \mathbf{B}\mathbf{K}_{\mathrm{pc}}\mathbf{S}_{x,k})\Delta\mathbf{x}(k) - \frac{\alpha}{\beta}\mathbf{B}\mathbf{K}_{\mathrm{pc}}\mathbf{S}_{x,k-1}\Delta\mathbf{x}(k-1) + \delta\end{aligned} \tag{29}$$

where δ represents the sum of the items which do not include terms $\Delta\mathbf{x}(k)$ and $\Delta\mathbf{x}(k-1)$.

In steady state, $\Delta\mathbf{x}(k) = \Delta\mathbf{x}(k-1)$, while in a dynamic process, since the sampling frequency of current-loop is sufficiently small, $\Delta\mathbf{x}(k)$ and $\Delta\mathbf{x}(k-1)$ can still be assumed equal in successive sampling periods. Then, (29) can be transformed to

$$\begin{aligned}\Delta\mathbf{x}(k+1) &= \mathbf{A}\Delta\mathbf{x}(k) + \mathbf{B}\Delta\mathbf{u}(k) \\ &= (\mathbf{A} - \mathbf{B}\mathbf{K}_{\mathrm{pc}}\mathbf{S}_{x,k} - \frac{\alpha}{\beta}\mathbf{B}\mathbf{K}_{\mathrm{pc}}\mathbf{S}_{x,k-1})\Delta\mathbf{x}(k) + \delta \\ &= \mathbf{M}\Delta\mathbf{x}(k) + \delta.\end{aligned} \tag{30}$$

The dimension of $\mathbf{M}$ is 2×2. Assuming the two eigenvalues of $\mathbf{M}$ as λ_1 and λ_2, λ_1 and λ_2 are conjugate and can be expressed as

$$\lambda_1 = \lambda_{\mathrm{real}} + j\lambda_{\mathrm{image}}\lambda_2 = \lambda_{\mathrm{real}} - j\lambda_{\mathrm{image}} \tag{31}$$

where λ_{real} and λ_{image} represent the real and image parts of the eigenvalues, respectively.

The stability condition is that all the eigenvalues of matrix $\mathbf{M}$ must be located within the unit circle, which can be expressed as

$$P = \sqrt{\lambda_{\mathrm{real}}{}^2 + \lambda_{\mathrm{image}}{}^2} < 1. \tag{32}$$

P is the amplitude of the eigenvalue, where if $P < 1$, the whole system will be asymptotically stable. For the 750 W SPMSM used in this paper, the motor parameters are shown in Table I. Only β determines the value of P. The relationship between P and β is plotted in Fig. 3 and demonstrates that only if $\beta > 0.45$, will $P < 1$, which means the system is stable. This is a critical rule for selecting α and β.

TABLE I
MAIN PARAMETERS OF 750 W PMSM

Parameter	Symbol	Rated Value
Motor Power	P_0	750 W
Motor Torque	T_0	2.39 N·m
Motor Speed	n_0	3000 r/min
Phase Current	I_0	3 A
Poles	p_0	4
Stator Resistance	R_0	2.88 Ω
Stator Inductance	L_0	3.9 mH
Flux Linkage of Magnet	ψ_{f0}	0.13 Wb
Inertia	J_0	1.82×10^{-3} kg·m^2

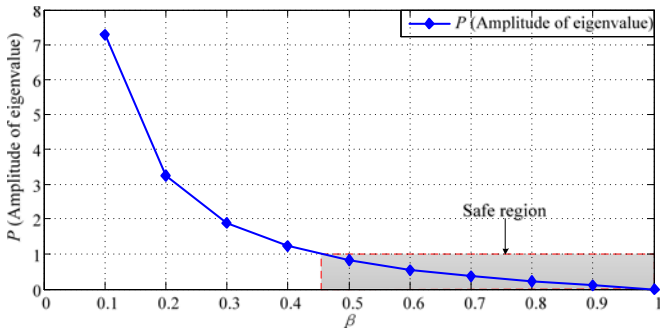

Fig. 3. Relationship between P and β.

B. Disturbance Rejection

Multistep prediction of R-PPC can improve disturbance rejection ability compared with conventional PPC because more information will be incorporated with a larger prediction horizon. Moreover, introducing current at the $(k-1)th$ instant into R-PPC can also improve disturbance rejection ability. The effect of load disturbances T_L on the motor speed can be evaluated via transfer functions. The speed-loop diagram is shown in Fig. 4,

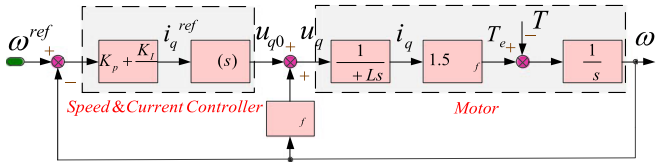

Fig. 4. Diagram of speed-loop with R-PPC.

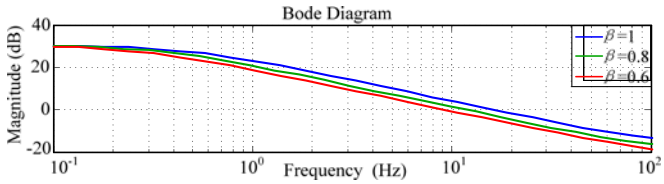

Fig. 5. Frequency characteristic with different β (input: T_L, output: ω).

in which the speed-loop controller is a PI regulator. K_p and K_I are proportional and integral coefficients, respectively, and correspond to experimental setup with $K_p = 20$ and $K_I = 0.025$. The effect of α and β against load disturbance is analyzed in this part.

The q-axis current state equation in discrete form according to (2) is

$$i_q{}^{ref}(k+1) = -T\omega_e(k)i_d(k) + \left(1 - \frac{TR}{L}\right) i_q(k) + \frac{T}{L}u_q(k) - \frac{T\psi_f\omega_e(k)}{L}. \quad (33)$$

In Fig. 4, $F(s)$ is the transfer function of current-loop without the term ψ_f. i_q^{ref} and u_{q0} are the input and output, respectively. In R-PPC, since the prediction process is based on currents measured at the $(k-1)$th and kth instants, $i_q(k)$ can be substituted approximately as $\alpha i_q(k-1) + \beta i_q(k)$. For the used SPMSM, i_d is controlled as 0, and the R-PPC performance guarantees $i_q^{ref} \approx i_q$. Thus, the discrete transfer function can be obtained from (33)

$$F(z) = \frac{u_{q0}(z)}{i_q{}^{ref}(z)} = \frac{L}{T}\left[z - \left(1 - \frac{TR}{L}\right)(z^{-1}\alpha + \beta)\right]. \quad (34)$$

The relationship between Z domain and S domain is $z = e^{sT}$. When T is sufficiently small, $z \approx 1 + sT$, thence the continuous transfer function from (34) is

$$F(s) = \frac{L}{T}\left[1 + sT - \left(1 - \frac{TR}{L}\right)\left(\frac{\alpha}{1+sT} + \beta\right)\right]. \quad (35)$$

In order to evaluate the influence of T_L on speed, the system should be considered with T_L as the input and ω as the output, whence the influence of T_L on ω is elicited. Then, the transfer function is obtained according to Fig. 4

$$G(s) = \frac{\omega(s)}{T_L(s)} = \frac{1}{\left[p\psi_f - \left(K_p + \frac{K_I}{s}\right)F(s)\right]K_T/(R+Ls) - Js} \quad (36)$$

The motor parameters are those in Table I. The amplitude characteristics with different α and β values are plotted in the Bode diagram in Fig. 5 according to (36).

Fig. 5 shows that through appropriately reducing β, the gain magnitude can be reduced. Smaller gain magnitude means that the speed fluctuation ω is also small under the same load disturbance T_L. In other words, antidisturbance ability can be enhanced when β makes the gain magnitude small.

Fig. 6. Experimental platform of 750 W PMSM drive. (a) Load test platform. (b) PMSM driver system.

As shown in Fig. 5, the gain magnitude is relatively small when $\beta = 0.6$. However, if β is too small, it will result in an unstable system according to Fig. 3. The stability of a practical system is of foremost importance; therefore, a reasonable tradeoff between disturbance rejection ability and stability should be reached.

In the following simulations and experimentation, α and β are 0.2 and 0.8, which guarantee system stability, and also achieve the desired disturbance rejection ability.

V. Simulation and Experimental Results

A. Experimental Setup

The main PMSM parameters are presented in Table I and the laboratory platform is shown in Fig. 6. It is composed of two 750 W PMSM motors (drive and load machines), each is controlled by TMS320F28335 DSP. The 310 V dc buses of the drive motor and load motor are parallel connection and load motor provides load torque. The current-loop sampling frequency is 10 kHz and that of the speed-loop is 1 kHz. During the experimentation, crucial variables are output to a digital oscilloscope through DA converters on the control board. Only stator current is directly measured by current probe.

Current and voltage restrictions are necessary to guarantee the safety of the system. The effective limitation approach proposed in [38], to constrain current and voltage, is adopted. To be specific, a rectangular region has been enforced to independently limit i_d and i_q

$$i_d \in [-\sigma I_{\max}\ \sigma I_{\max}] \quad i_q \in [-I_{\max}\ I_{\max}]$$

where $I_{\max}$ is the maximum value of dq-axis currents. σ is a coefficient chosen as 0.2 since i_d is kept as zero.

As regards the voltage limit, an octagon P_8 approximation is used to enforce eight linear constraints. The octagon region is

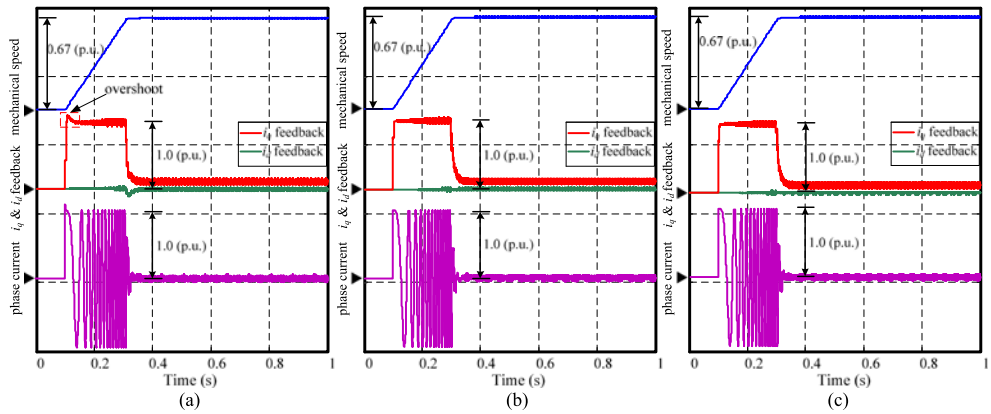

Fig. 7. Simulation comparison of the three methods. (a) PI current regulator. (b) Conventional PPC. (c) R-PPC.

circumscribed into a circular limit region

$$\mathbf{u} \in P_8 \subset \{\mathbf{u} : |\mathbf{u}| \leq U_{\max}\}$$

where $\mathbf{u}$ is the control voltage vector generated by the composition of u_d and u_q. $U_{\max}$ is maximum voltage determined by the dc link voltage. In this paper, the R-PPC has been designed to enforce a voltage limit of 180 V (dc bus at 310 V).

In following experimentation, the speed-loop uses a PI controller with $K_P = 20$ and $K_I = 0.025$; tuned using the Ziegler–Nichols method. It has an antiwindup structure, with an antiwindup parameter of $K_C = 0.05$. The response of the ESO should be as fast as current-loop to provide sufficiently accurate estimated states and uncertainties for R-PPC. Generally, the bandwidth of current-loop is around 1 kHz. Hence, in this paper, the bandwidth ω_c of the ESO is chosen as 1 kHz, which is fast enough to provide estimated states to the R-PPC. In the simulation and experimental figures, waveforms are normalized by taking the rated value as reference.

B. Performance Comparison of PI, Conventional PPC, and R-PPC

First, the system performance when the current-loop uses PI, conventional PPC, and R-PPC is compared. Current-loop PI parameters are tuned to optimal. Motor parameters used in the PPC ($R_{\rm PPC}$, $L_{\rm PPC}$, and $\psi_{\rm f-PPC}$) and R-PPC ($R_{\rm R-PPC}$, $L_{\rm R-PPC}$) are rated. All the controllers operate with same optimal speed-loop PI controller.

The simulation results are shown in Fig. 7 and the experimental results are shown in Fig. 8, where speed feedback, *dq*-axis currents, and phase current are shown.

The results reflect that when the three controllers are appropriately tuned, all behave giving the desired current control performance. In a transient process, i_q can be restrained to its limit (1.0 p.u.), and the phase current magnitude is also limited to 1 p.u. i_d is controlled to 0 in all cases. However, in a transient process, i_q of PI controller shows slight overshoot, unlike i_q with PPC and R-PPC. This demonstrates predictive controllers have better dynamic current performance than a PI controller.

C. Flux Robustness Comparison Between Conventional PPC and R-PPC

The influence of rotor flux mismatch simulation results is shown in Fig. 9 and the experimental results are shown in Fig. 10. The speed feedback, *q*-axis currents reference and feedback, and phase current are shown.

Figs. 9(a) and 10(a) show the simulated and experimental results of conventional PPC when $\psi_{\rm f-PPC}$ is double of the real flux ψ_{f0}. Inductance $L_{\rm PPC}$ and resistance $R_{\rm PPC}$ are set to rated value. In the transient process, i_q feedback is larger than the limit (1 p.u.). This may result in system overcurrent. In addition, an apparent static error between i_q reference and the feedback can be observed. These results are consistent with [27], reflecting that conventional PPC is sensitive to rotor flux, as its mismatch deteriorates current performance.

Figs. 9(b) and 10(b) show the simulated and experimental results of R-PPC, which operates without rotor flux since it is based on an incremental model. Other motor parameters, inductance $L_{\rm R-PPC}$ and resistance $R_{\rm R-PPC}$ are set to rated value as with the conventional PPC case. Other parameters are $\alpha = 0.2$, $\beta = 0.8$, as presented in Section IV-B. The waveforms demonstrate that with R-PPC, i_q feedback can track its reference accurately, without any rotor flux knowledge.

D. Inductance Robustness Comparison Between Conventional PPC and R-PPC

The robustness of inductance mismatch is compared between conventional PPC and R-PPC. The simulation results are shown in Fig. 11 and the experimental results are shown in Fig. 12, with speed feedback, *dq*-axis currents feedback, and phase current shown.

Figs. 11(a) and 12(a) show the simulation and experimental results of conventional PPC when $L_{\rm PPC}$ is 2.5 times of the rated value. Rotor flux $\psi_{\rm f-PPC}$ and resistance $R_{\rm PPC}$ are set to rated value. The results of conventional PPC show severe oscillation of *dq*-axis currents and phase currents, where the current is not controlled.

Figs. 11(b) and 12(b) show the simulation and experimental results of R-PPC when $L_{\rm R-PPC}$ is again set 2.5 times of the

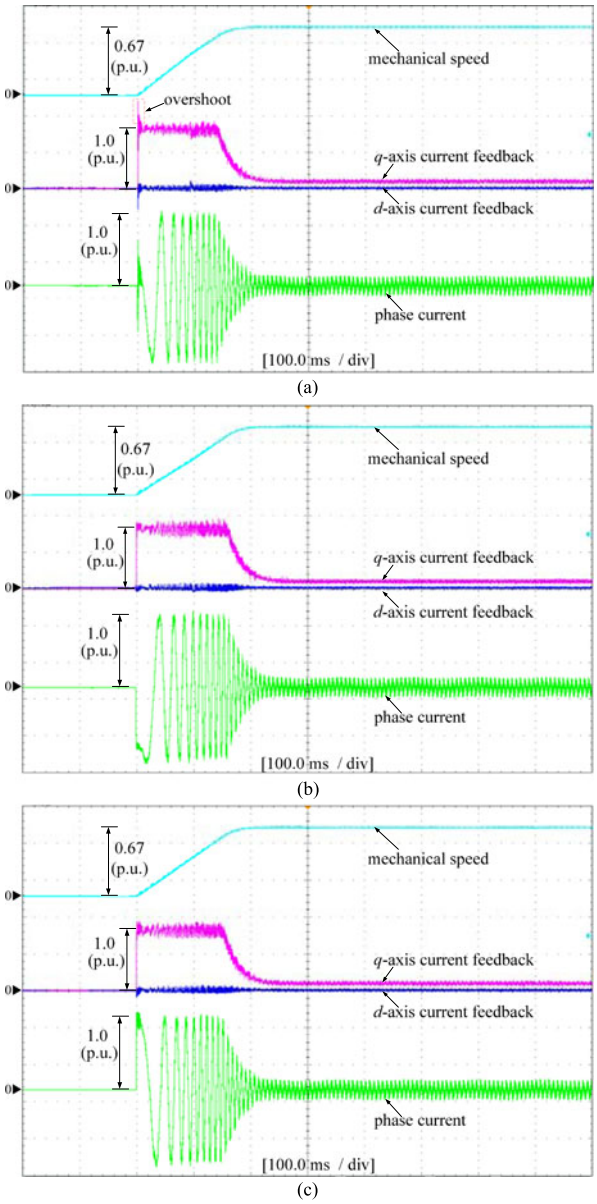

Fig. 8. Experimental comparison of the three methods. (a) PI current regulator. (b) Conventional PPC. (c) R-PPC.

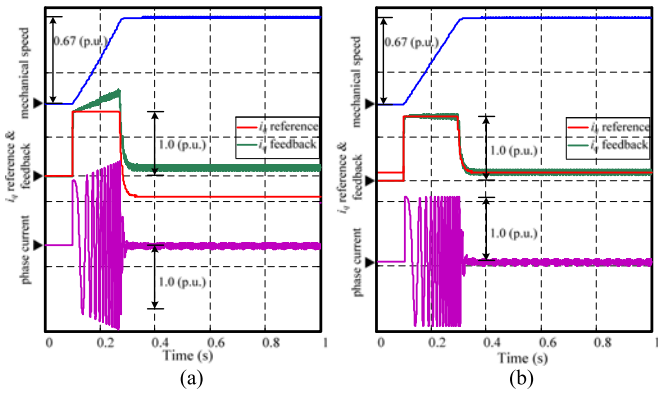

Fig. 9. Simulation results of rotor flux robustness comparison between conventional PPC and R-PPC. (a) $\psi_{\mathrm{f-PPC}} = 2\psi_{f0}$. (b) R-PPC.

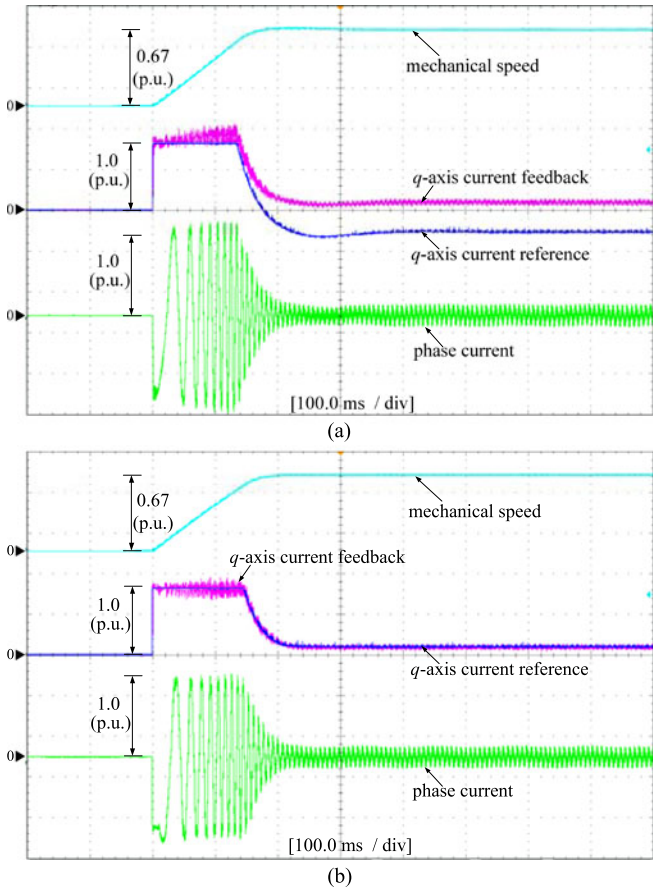

Fig. 10. Experimental results of rotor flux robustness comparison between conventional PPC and R-PPC. (a) $\psi_{\mathrm{f-PPC}} = 2\psi_{f0}$. (b) R-PPC.

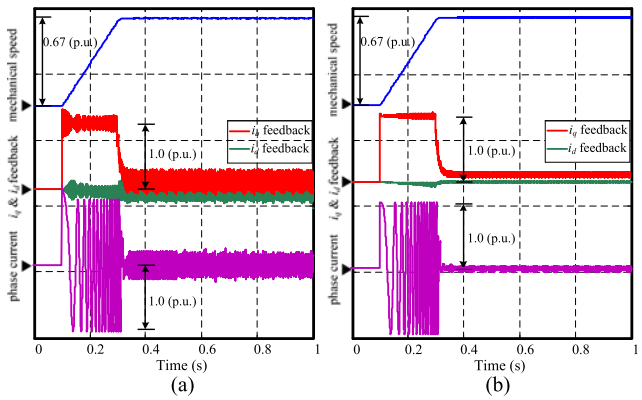

Fig. 11. Simulation results of inductance robustness comparison between conventional PPC and R-PPC. (a) $L_{\mathrm{PPC}} = 2.5L_0$. (b) $L_{\mathrm{R-PPC}} = 2.5L_0$.

rated value. Resistance $R_{\mathrm{R-PPC}}$ is equal to rated value. The R-PPC results demonstrate that the *dq*-axis currents and phase current remain stable and behave with excellent dynamic and steady performance even though inductance mismatch occurs. The results verify the effectiveness of ESO in improving robustness against inductance mismatch.

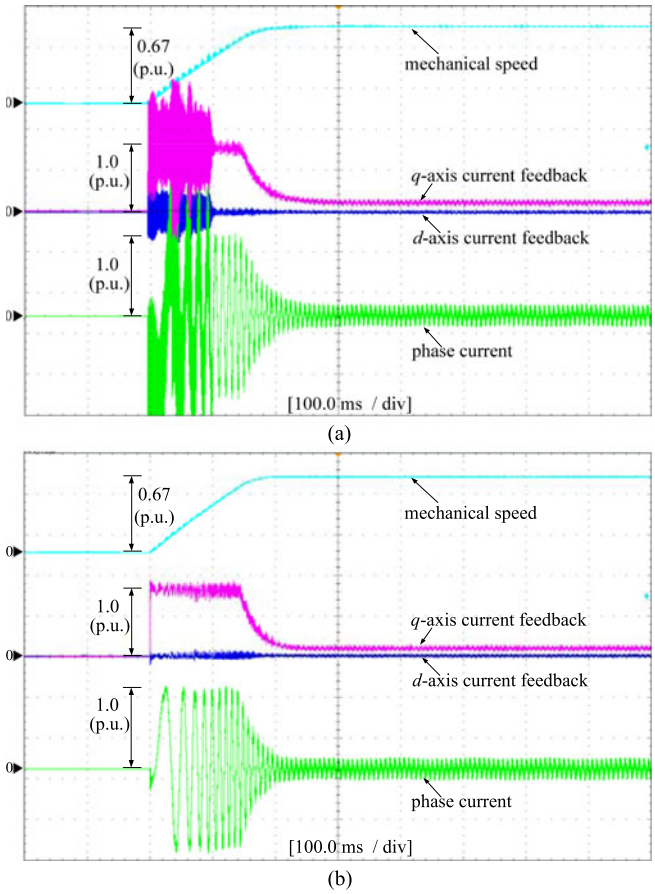

Fig. 12. Experimental results of inductance robustness comparison between conventional PPC and R-PPC. (a) $L_{\mathrm{PPC}} = 2.5L_0$. (b) $L_{\mathrm{R-PPC}} = 2.5L_0$.

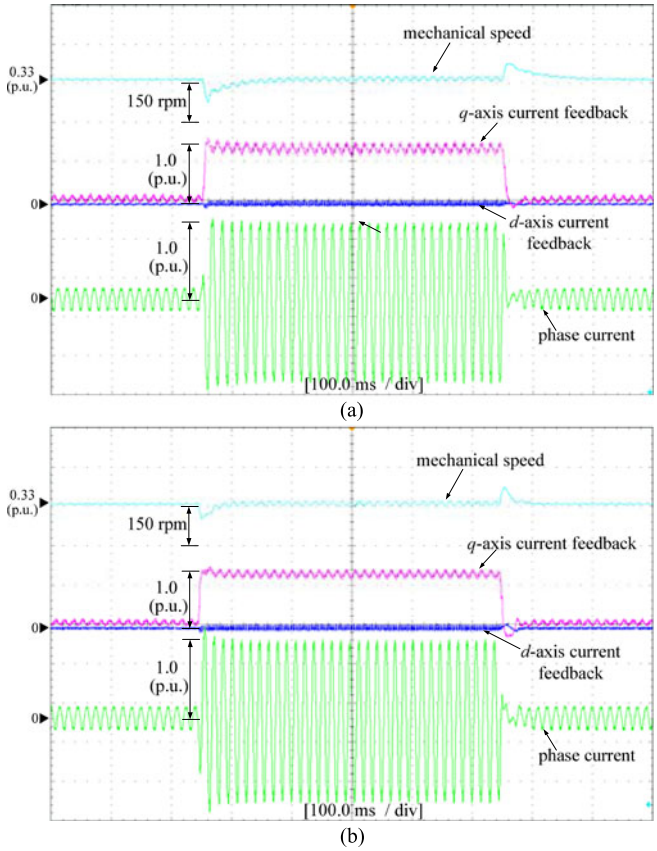

Fig. 14. Experimental results of disturbance rejection comparison between conventional PPC and R-PPC. (a) Conventional PPC with rated load. (b) R-PPC with rated load.

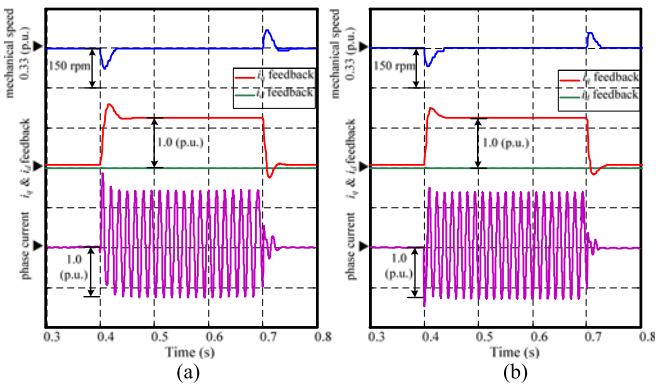

Fig. 13. Simulation results of disturbance rejection comparison between conventional PPC and R-PPC. (a) Conventional PPC with rated load. (b) R-PPC with rated load.

E. Disturbance Rejection Comparison Between Conventional PPC and R-PPC

Figs. 13 and 14 show the simulation and experimental responses of conventional PPC and R-PPC controllers to rated load, respectively. Rated motor parameters are used in conventional PPC and R-PPC, while other R-PPC parameters are: $\alpha = 0.2$, $\beta = 0.8$. Fig. 13 reflects that in simulation, R-PPC speed fluctuation is approximately 68 r/min, while that with conventional PPC is 75 r/min, when suddenly adding or removing load. The experimental results shown in Fig. 14 demonstrate that R-PPC speed fluctuation is approximately 70 r/min while that with conventional PPC is 84 r/min. The recovery time of speed with R-PPC is also shorter than that with conventional PPC. These results show R-PPC has better disturbance rejection ability due to multistep prediction and the introduction of $\mathbf{x}(k-1)$. These results are consistent with the theoretical analysis in Section IV-B.

F. Speed Reversal of R-PPC

The simulation and experimental results of speed reversal responses of the system are reported in Fig. 15, where the motor is forced to reverse its direction. The system operates in a regenerative mode until the speed of rotor is positive; and thereafter, the system switches to motoring mode until the rotor speed reaches reference. The simulation result shown in Fig. 15(a) and experiment result shown in Fig. 15(b) both demonstrate good dynamic and steady response of currents. In addition, currents show such a good behavior without exceeding the current limitation (1.0 p.u.).

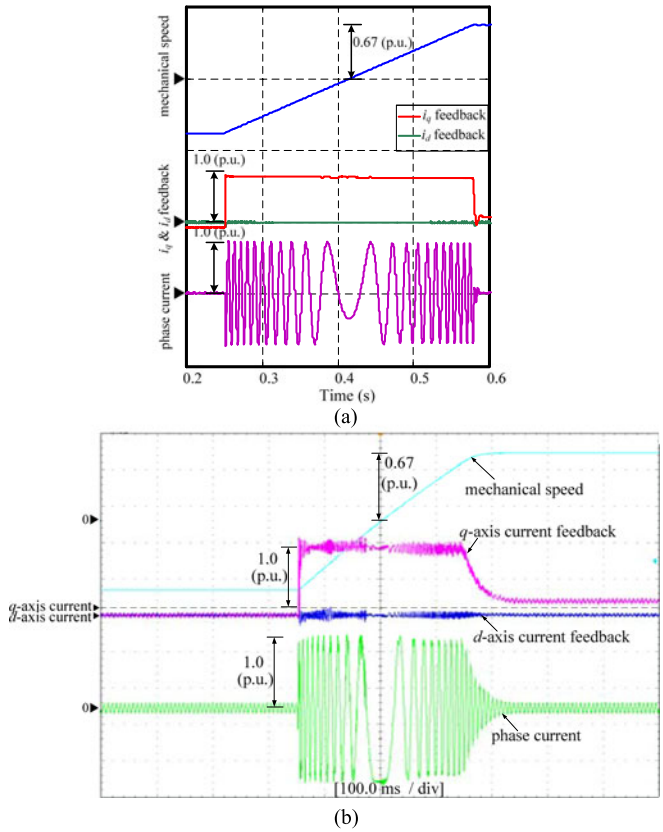

Fig. 15. Simulation and experimental responses of speed reversal with R-PPC. (a) Simulation. (b) Experimental.

TABLE II
AVERAGE EXECUTION TIMES OF THE CONVENTIONAL PPC AND R-PPC WITH CURRENT-LOOP SAMPLING INTERVAL $T = 100\,\mu$S.

Time	Conventional PPC (μs)	Time	R-PPC (μs)
$t_{\rm m}$	6.34	t_m	6.34
$t_{\rm opt}$	9.40	$t_{\rm pre}$	8.05
Null	0	$t_{\rm ESO}$	7.82
Null	0	$t_{\rm opt}$	7.56
Total	15.74	Total	29.77

TABLE III
COMPARISON OF MEAN SQUARED ERROR OF THE CURRENT TRACKING BETWEEN THE CONVENTIONAL PPC AND R-PPC

Steady State ($T_L = 0$ Nm)			Controller Type	
Speed	$L_{\rm PPC}, L_{\rm R-PPC}, \psi_{\rm f-PPC}$	MSE	PPC	R-PPC
300 r/min	$L_{\rm PPC} = L_0, \psi_{\rm f-PPC} = \psi_{f0}$	MSE $(i_q{}^* - i_q)$	0.153	0.158
	$L_{\rm R-PPC} = L_0$	MSE $(i_d{}^* - i_d)$	0.051	0.048
	$L_{\rm PPC} = L_0, \psi_{\rm f-PPC} = 2\psi_{f0}$	MSE $(i_q{}^* - i_q)$	0.259	0.160
	$L_{\rm R-PPC} = L_0$	MSE $(i_d{}^* - i_d)$	0.056	0.051
	$L_{\rm PPC} = 2.5L_0, \psi_{\rm f-PPC} = \psi_{\rm f0}$	MSE $(i_q{}^* - i_q)$	0.552	0.173
	$L_{\rm R-PPC} = 2.5L_0$	MSE $(i_d{}^* - i_d)$	0.225	0.062
2000 r/min	$L_{\rm PPC} = L_0, \psi_{\rm f-PPC} = \psi_{f0}$	MSE $(i_q{}^* - i_q)$	0.171	0.178
	$L_{\rm R-PPC} = L_0$	MSE $(i_d{}^* - i_d)$	0.068	0.063
	$L_{\rm PPC} = L_0, \psi_{\rm f-PPC} = 2\psi_{f0}$	MSE $(i_q{}^* - i_q)$	1.422	0.176
	$L_{\rm R-PPC} = L_0$	MSE $(i_d{}^* - i_d)$	0.071	0.065
	$L_{\rm PPC} = 2.5L_0, \psi_{\rm f-PPC} = \psi_{f0}$	MSE $(i_q{}^* - i_q)$	0.742	0.188
	$L_{\rm R-PPC} = 2.5L_0$	MSE $(i_d{}^* - i_d)$	0.373	0.074

G. Comparison of Computational Cost and Mean Square Error

Since R-PPC has a larger prediction horizon than with conventional PPC and ESO is combined with R-PPC, the computational burden of the proposed controller will be considerable. In order to evaluate and compare the computation cost when a DSP executes PPC and R-PPC, the processing time of each stage is calculated considering 2000 iterations, and measured by counting the reference-pulses (at 150 MHz) of the DSP TMS320F28335. In conventional PPC, the time demanded for current and speed measurement, and for the speed-loop controller to generate $i_{\rm q}$ reference is $t_m = 6.34\ \mu$s. The time required for current prediction and optimal voltage vector calculation is $t_{\rm opt} = 9.40\ \mu$s. In the proposed R-PPC, t_m is the same as that with conventional PPC, while the time required for the ESO to generate estimated *dq*-axis currents and disturbances is $t_{\rm ESO} = 7.82\ \mu$s. The time needed for current prediction is $t_{\rm pre} = 8.05\ \mu$s and for the calculation of optimal voltage increment, $t_{\rm opt} = 7.56\,\mu$s. Therefore, the total processing time for each conventional PPC cycle is $t_{\rm PPC} = t_m + t_{\rm opt} = 15.74\ \mu$s, while for each R-PPC cycle, $t_{\rm R-PPC} = t_m + t_{\rm pre} + t_{\rm ESO} + t_{\rm opt} = 29.77\ \mu$s. The experimental results are shown in Table II, and these results reflect the main shortcoming of the R-PPC controller: the computational cost is almost twice that of the conventional PPC. However, considering the current-loop sampling interval is 100 μs, the additional computational cost caused by multistep prediction and ESO is still manageable for the DSP.

In order to quantitatively compare the performance of conventional PPC and R-PPC, the root mean square error (MSE) quantity (defined as the following equation) is utilized:

$$\mathrm{MSE}(x^{ref} - x) = \sqrt{\frac{1}{N}\sum_{j=1}^{N}\left(x^{ref} - x_j\right)^2}. \tag{37}$$

The MSEs of the tracking error of the *dq*-axis currents are defined as $\mathrm{MSE}(i_d^{ref} - i_d)$ and $\mathrm{MSE}(i_q^{ref} - i_q)$. The MSE experimental results are demonstrated in Table III, which are obtained at different operating points (300 and 2000 r/min, respectively) without load. The main comparison conclusions include:

1) when $L_{\rm PPC}$ and $\psi_{\rm f-PPC}$ are set to rated value in conventional PPC, the MSEs are similar to R-PPC.
2) when $\psi_{\rm f-PPC}$ with conventional PPC is set to double of the rated value, the MSE($i_{\rm d}{}^{ref} - i_{\rm d}$) is almost unchanged, whereas the $\mathrm{MSE}(i_q^{ref} - i_q)$ of PPC is much larger than that of R-PPC because of the static error between the i_q reference and its feedback in PPC.
3) when inductance in conventional PPC and R-PPC is set to 2.5 times of the rated value, $\mathrm{MSE}(i_d^{ref} - i_d)$ and $\mathrm{MSE}(i_q^{ref} - i_q)$ are both larger than those of R-PPC. This is because the equivalent error voltages caused by inductance mismatch have been compensated by ESO.

These results reflect R-PPC has better current control than conventional PPC where parameters mismatch occurs, and the conclusions are consistent with the demonstrated simulation and experimental results.

VI. Conclusion

A robust PWM predictive current control algorithm for PMSM drives, called R-PPC, has been proposed. Compared with conventional PPC, an R-PPC controller operates well in transient and steady processes without rotor flux since it adopts an incremental model. This modification is easier to be implemented than other complex identification or flux observers. In addition, the prediction horizon is enlarged into 3 and the $(k-1)$th currents are used in R-PPC in order to achieve better disturbance rejection performance. An ESO is combined with R-PPC to solve inductance mismatch issues. Detailed theoretical analyses about stability and disturbance rejection ability have been given in quantitative form, and the rule for selecting appropriate α and β has been presented. The simulation and experimental results confirm the proposed R-PPC achieves good performance without rotor flux, and can effectively enhance robustness against inductance mismatch and disturbance variation.

References

[1] R. D. Lorenz, "Robotics and automation applications of drives and converters," *Proc. IEEE*, vol. 89, no. 6, pp. 951–962, Jun. 2001.

[2] Y. Kwon, S. Kim, and S. Sul, "Six-step operation of PMSM with instantaneous current control," *IEEE Trans. Ind. Appl.*, vol. 50, no. 4, pp. 2614–2625, Jul./Aug. 2014.

[3] P. Cortes, M. P. Kazmierkowski, R. M. Kennel, D. E. Quevedo, and J. Rodriguez, "Predictive control in power electronics and drives," *IEEE Trans. Ind. Electron.*, vol. 55, no. 12, pp. 4312–4324, Dec. 2008.

[4] B. Kou, C. Li, and S. Cheng, "Flux-weakening-characteristic analysis of a new permanent-magnet synchronous motor used for electric vehicles," *IEEE Trans. Plasma Sci.*, vol. 39, no. 1, pp. 511–515, Jan. 2011.

[5] J. S. Lee and R. D. Lorenz, "Deadbeat direct torque and flux control of IPMSM drives using a minimum time ramp trajectory method at voltage and current limits," *IEEE Trans. Ind. Appl.*, vol. 50, no. 6, pp. 3795–3804, Nov./Dec. 2014.

[6] H. T. Moon, H. S. Kim, and M. J. Youn, "A discrete-time predictive current control for PMSM," *IEEE Trans. Power Electron.*, vol. 18, no. 1, pp. 464–472, Jan. 2003.

[7] M. Florent and L. Xuefang, "A comparative study of predictive current control schemes for a permanent-magnet synchronous machine drive," *IEEE Trans. Ind. Electron.*, vol. 56, no. 7, pp. 2715–2728, Apr. 2009.

[8] M. P. Kazmierkowski and L. Malesani, "Current control techniques for three-phase voltage-source PWM converters: A survey," *IEEE Trans. Ind. Electron.*, vol. 45, no. 5, pp. 691–703, Oct. 1998.

[9] H. Lin, T. A. Lipo, B. I. Kwon, and S. R. Cheon, "Three-level hysteresis current control for a three-phase permanent magnet synchronous motor drive," in *Proc. 7th Int. Power Electron. Motion Control Conf.*, Jun. 2012, pp. 1004–1008.

[10] H. Mao, X. Yang, Z. Chen, and Z. Wang, "A hysteresis current controller for single-phase three-level voltage source inverters," *IEEE Trans. Power Electron.*, vol. 27, no. 7, pp. 3330–3339, Jan. 2012.

[11] P. Karamanakos, P. Stolze, R. M. Kennel, S. Manias, and H. du Toit Mouton, "Variable switching point predictive torque control of induction machines," *IEEE Trans. Emerg. Sel. Topics Power Electron.*, vol. 2, no. 2, pp. 285–295, Jun. 2014.

[12] J. Scoltock, T. Geyer, and U. Madawala, "Model predictive direct power control for grid-connected NPC converters," *IEEE Trans. Ind. Electron.*, vol. 62, no. 9, pp. 5319–5328, Sep. 2015.

[13] B. S. Riar, T. Geyer, and U. K. Madawala, "Model predictive direct current control of modular multilevel converters: Modeling, analysis, and experimental evaluation," *IEEE Trans. Power Electron.*, vol. 30, no. 1, pp. 431–439, Jan. 2015.

[14] M. Preindl and E. Schaltz, "Sensorless model predictive direct current control using novel second-order PLL observer for PMSM drive systems," *IEEE Trans. Ind. Electron.*, vol. 58, no. 9, pp. 4087–4095, Aug. 2011.

[15] W. Xu, R. Qu, and W. Yang, "New model based predictive current control strategy for doubly salient permanent magnet synchronous machines," in *Proc. 2013 IEEE Energy Convers. Congr. Expo.*, Sep. 2013, pp. 1450–1457.

[16] C.-K. Lin, T.-H. Liu, J. T. Yu, L.-C. Fu, and C.-F. Hsiao, "Model-free predictive current control for interior permanent-magnet synchronous motor drives based on current difference detection technique," *IEEE Trans. Ind. Electron.*, vol. 61, no. 2, pp. 667–681, Feb. 2014.

[17] S. Mariethoz, A. Domahidi, and M. Morari, "Sensorless explicit model predictive control of permanent magnet synchronous motors," in *Proc. 2009 IEEE Int. Electr. Mach. Drives Conf.*, May 2009, pp. 1250–1257.

[18] W. Xie *et al.*, "Finite control set-model predictive torque control with a deadbeat solution for PMSM drives," *IEEE Trans. Ind. Electron.*, vol. 62, no. 9, pp. 5402–5410, Mar. 2015.

[19] C. Lim, E. Levi, M. Jones, N. A. Rahim, and W. P. Hew, "FCS-MPC-based current control of a five-phase induction motor and its comparison with PI-PWM control," *IEEE Trans. Ind. Electron.*, vol. 61, no. 1, pp. 149–163, Jan. 2014.

[20] W. Sun, Y. Yu, D. Xu, J. Xu, and L. Ding, "Predictive current control method in induction motor speed sensorless drive," in *Proc. IEEE Power Electron. Conf.*, May 2014, pp. 341–345.

[21] A. Piippo, M. Hinkkanen, and J. Luomi, "Adaptation of motor parameters in sensorless PMSM drives," *IEEE Trans. Ind. Appl.*, vol. 45, no. 1, pp. 203–212, Jan. 2009.

[22] K. Liu and Z. Zhu, "Mechanical parameter estimation of permanent-magnet synchronous machines with aiding from estimation of rotor pm flux linkage," *IEEE Trans. Ind. Appl.*, vol. 51, no. 4, pp. 3115–3125, Jul./Aug. 2015.

[23] S. J. Underwood and I. Husain, "On-line parameter estimation and adaptive control of permanent magnet synchronous machines," *IEEE Trans. Ind. Electron.*, vol. 57, no. 7, pp. 2435–2443, Jul. 2010.

[24] M. N. Uddin and M. M. I. Chy, "Online parameter-estimation-based speed control of PM ac motor drive in flux-weakening region," *IEEE Trans. Ind. Appl.*, vol. 44, no. 5, pp. 1486–1494, Sep./Oct. 2008.

[25] K. Liu and Z. Zhu, "Quantum genetic algorithm-based parameter estimation of PMSM under variable speed control accounting for system identifiability and VSI nonlinearity," *IEEE Trans. Ind. Electron.*, vol. 62, no. 4, pp. 2363–2371, Aug. 2015.

[26] K. Liu and Z. Zhu, "Online estimation of the rotor flux linkage and voltage-source inverter nonlinearity in permanent magnet synchronous machine drives," *IEEE Trans. Power Electron.*, vol. 29, no. 1, pp. 418–427, Jan. 2014.

[27] G. Wang, M. Yang, L. Niu, X. Gui, and D. Xu, "Improved predictive current control with static current error elimination for permanent magnet synchronous machine," in *Proc. 40th Annu. Conf. IEEE Ind. Electron. Soc.*, Oct./Nov. 2014, pp. 661–667.

[28] L. Niu, M. Yang, and D. Xu, "An adaptive robust predictive current control for PMSM with online inductance identification," *Proc. IREE*, vol. 7, no. 2, pp. 3845–3856, 2012.

[29] W. Wang, X. Xiao, and Y. Ding, "An adaptive incremental predictive current control method of PMSM," in *Proc. 2013 15th Eur. Conf. Power Electron. Appl.*, Sep. 2013, pp. 1–8.

[30] K. Wiedmann and A. Mertens, "Novel MRAS approach for online identification of key parameters for self-sensing control of PM synchronous machines," in *Proc. IEEE 15th Int. Power Electron. Motion Control Conf.*, Sep. 2012, pp. LS4b-1.2-1–LS4b-1.2-8.

[31] C. Xia, M. Wang, Z. Song, and T. Liu, "Robust model predictive current control of three-phase voltage source PWM rectifier with online disturbance observation," *IEEE Trans. Ind. Informat.*, vol. 8, no. 3, pp. 459–471, Jan. 2012.

[32] G. Wang, Y. Wang, J. Xu, N. Zhao, and D. Xu, "Weight-transducerless rollback mitigation adopting enhanced MPC with extended state observer for direct-drive elevators," *IEEE Trans. Power Electron.*, vol. 31, no. 6, pp. 4440–4451, Jan. 2016.

[33] D. J. Vaghela and H. N. Chaudhari, "Investigation of design, analysis and performance of hysteresis current control PMSM drive," in *Proc. 2015 Int. Conf. Electr., Electron., Signals, Commun. Optim.*, 2015, pp. 1–6.

[34] A. Dey, P. P. Rajeevan, R. Ramchand, K. Mathew, and K. Gopakumar,"A space-vector-based hysteresis current controller for a general n-level inverter-fed drive with nearly constant switching frequency control," *IEEE Trans. Ind. Electron.*, vol. 60, no. 5, pp. 1989–1998, May 2013.
[35] T. S. Gabbi, H. A. Grundling, and R. P. Vieira, "Current controller for sensorless PMSM drive using combined sliding mode strategy and disturbance observer," in *Proc. 41st Annu. Conf. IEEE Ind. Electron. Soc.*, 2015, pp. 003773–003778.
[36] J. C. Moreno, J. M. Espi Huerta, R. G. Gil, and S. A. Gonzalez, "A robust predictive current control for three-phase grid-connected inverters," *IEEE Trans. Ind. Electron.*, vol. 56, no. 6, pp. 1993–2004, Jun. 2009.
[37] J. Rodas, F. Barrero, M. R. Arahal, C. Martín, and R. Gregor, "Online estimation of rotor variables in predictive current controllers: A case study using five-phase induction machines," *IEEE Trans. Ind. Electron.*, vol. 63, no. 9, pp. 5348–5356, Sep. 2016.
[38] S. Bolognani, L. Peretti, and M. Zigliotto, "Design and implementation of model predictive control for electrical motor drives," *IEEE Trans. Ind. Electron.*, vol. 56, no. 6, pp. 1925–1936, Jun. 2009.
[39] P. Cortes *et al.*, "Guidelines for weighting factors design in model predictive control of power converters and drives," in *Proc. 2009 IEEE Int. Conf. Ind. Technol.*, 2009, pp. 1–7.
[40] J. Q. Han, "From PID to active disturbance rejection control," *IEEE Trans. Ind. Electron.*, vol. 56, no. 3, pp. 900–906, Mar. 2009.
[41] H. J. Ahn and D. M. Lee, "A new bumpless rotor-flux position estimation scheme for vector-controlled washing machine," *IEEE Trans. Ind. Informat.*, vol. 12, no. 2, pp. 466–473, Apr. 2016.

Ming Yang (M'14) received the B.S., M.S., and Ph.D. degrees in electrical engineering from the Harbin Institute of Technology (HIT), Harbin, China, in 2000, 2002, and 2007, respectively.

In 2004, he, as a Lecturer, joined the Department of Electrical Engineering, HIT, where he has been a Professor of electrical engineering since 2016. From 2009 to 2012, he was a Postdoctoral Fellow at Shanghai STEP Electric Corporation. He has authored more than 60 technical papers published in journals and conference proceedings. He is the holder of 16 Chinese patents. His current major research interests include PMSM servo system, predictive current control, and mechanical resonance suppression.

Xiaoyu Lang received the B.S. degree in electrical engineering, in 2015, from the Harbin Institute of Technology, Harbin, China, where he is currently working toward the M.S. degree in power electronics and electrical drives in the School of Electrical Engineering and Automation.

His current research interests include PMSM servo system, predictive current control, and mechanical resonance suppression.

Jiang Long received the B.S. degree in electrical engineering and automation, in 2012, from the Chang Chun Institute of Technology, Chang Chun, China, and the M.S. degree in power electronics and electrical drives, in 2015, from the Harbin University of Science and Technology, Harbin, China, where he is currently working toward Ph.D. degree in power electronics and electrical drives in the School of Electrical Engineering and Automation.

His current research interest focuses on PMSM servo system.

Dianguo Xu (M'97–SM'12–F'16) was born in Heilongjiang, China, in 1960. He received the B.S. degree in control engineering from the Harbin Shipbuilding Engineering Institute, Harbin, China, in 1981, and the M.S. and Ph.D. degrees in electrical engineering from the Harbin Institute of Technology, Harbin, China, in 1984 and 1990, respectively.

Since 1994, he has been a Professor in the Department of Electrical Engineering, Harbin Institute of Technology. His current research interests include robotics, lighting electronics, power quality mitigation, consumer electronics, power electronics, and motor drives.

Dr. Xu is a member of the China Electrotechnical Society and China Power Supply Society.